Calibration of the Advanced X-ray Astrophysics Facility (AXAF): Project Science analyses

M. C. Weisskopf
NASA, Marshall Space Flight Center, ES01

R. F. Elsner, J. J. Kolodziejczak, S. L. O'Dell, M. E. Sulkanen, and A. F. Tennant
NASA, Marshall Space Flight Center, ES84

R. A. Austin, D. A. Swartz, and G. Zirnstein
USRA, Marshall Space Flight Center, ES84

(DRAFT: Editing is incomplete.)

Interim report

March 22, 1999

Abstract

This document is the interim report on Project Science analyses of data from the calibration of the Advanced X-ray Astrophysics Facility (AXAF). The report provides an introduction to AXAF calibration activities at the X-Ray Calibration Facility (XRCF) and then describes Project Science analyses of calibration data:

1. Beam-Normalization Detector (BND) data for X-ray Source System (XSS) monochromators;
2. Beam-uniformity data for X-ray Source System (XSS) monochromators;
3. Solid-State Detector (SSD) internal calibrator;
4. Solid-State Detector (SSD) continuum measurements;
5. Flight Contamination Monitor (FCM); and
6. Limits on High-Resolution Mirror Assembly (HRMA) contamination.

Contents

List of Figures

List of Tables

1 Flight Contamination Monitor

1.1 Objectives

The Advanced X-ray Astrophysics Facility (AXAF), the x-ray component of NASA's Great Observatories, underwent the most extensive, by far, system-level calibration program in the history of high-energy astrophysics at the Marshall Space Flight Center (MSFC) X-Ray Calibration Facility (XRCF) during the winter and spring of 1997 [1]. One of the key goals was to determine the absolute flux scale to an accuracy of a few percent or less, and detailed analysis of effective area measurements is continuing in order to achieve this goal for the ground calibration [2]. In addition, a high-fidelity ray trace program, maintained by the AXAF Mission Support Team and designed to model the performance of the High Resolution Mirror Assembly (HRMA) in great detail, will use the ground calibration results to predict the on-orbit performance. However, it is still important to verify the transfer of the ground-level calibration to on-orbit operation, particularly in view of the absence of any well characterized astronomical x-ray standard candles and the sensitivity of the AXAF effective area to changes in molecular (Fig. 1) and particulate contamination [3].

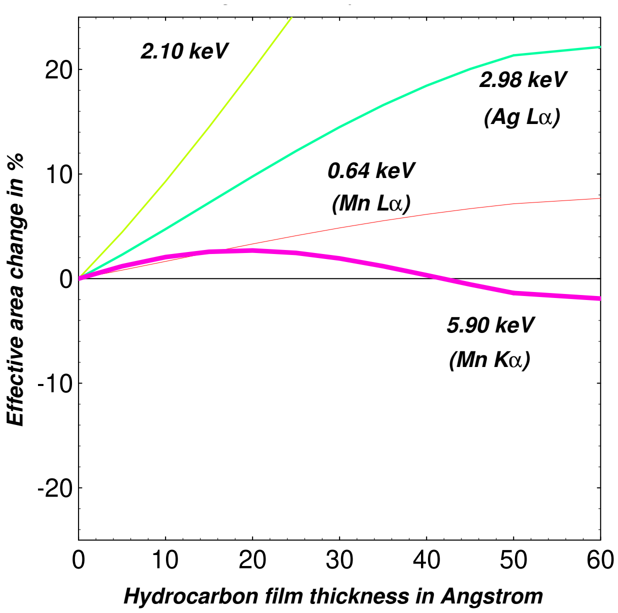

Figure 1: AXAF effective area changes in percent, at selected x-ray energies, as a function of the thickness of a uniform hydrocarbon film over 95% bulk density iridium.

For these reasons, a Flight Contamination Monitor system (FCM), made up of electron-capture radioactive sources emitting x-ray lines, is installed in the Forward Contamination Cover (FCC) of the HRMA (Fig. 2). There are four sources, spaced 90 deg apart, for each HRMA shell, with activities and radii scaled appropriately for that shell's aperture. The two objectives of the ground and in-orbit measurements using the FCM and focal plane detectors are these:

1. Verify the transfer of the HRMA flux scale from the XRCF test phase to the orbital-activation phase.

2. Measure or bound any changes in molecular contamination of the HRMA [3].

The focal plane detectors, the AXAF CCD Imaging Spectrometer (ACIS) and the High Resolution Camera (HRC), also employ their own radioactive calibration sources, in order to monitor any change in detector performance. During ground calibration FCM measurements were taken with ACIS, ACIS-2C

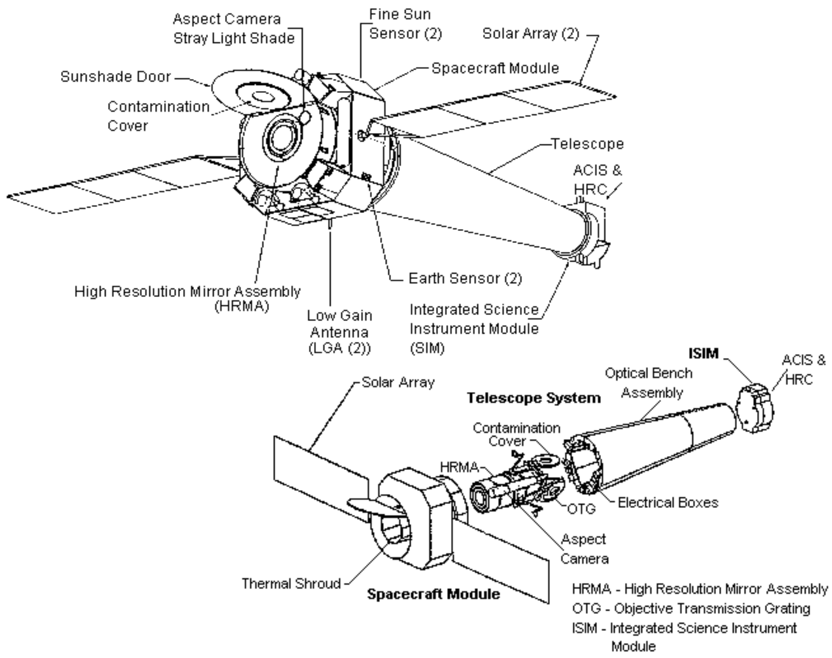

Figure 2: The AXAF spacecraft and components showing the FCC on the front of the HRMA. FCM measurements are taken during the activation phase with the FCC closed.

(an ACIS surrogate), and HRC-I (the imaging readout for HRC). The FCM measurements during the activation phase are the first look at the on-orbit HRMA/ACIS performance. Figure 3 is a schematic of the x-ray optical path for FCM measurements.

Each FCM source images the portion of the paraboloid aperture immediately in front of it, leading to an image of a slightly curved stripe in the focal plane. The FCM source 180 deg away contributes a stripe superimposed on the first one, but with a slight curvature in the opposite direction. The pair of FCM sources at 90 deg with respect to the first two contribute stripes perpendicular to the first two, leading to an image of a cross in the focal plane (Fig. 4). Although the global topology of the image is independent of energy, intensity contours depend slightly on energy due to the differing energy response of the four HRMA shells. Cross-correlation of measured and simulated images provides a measure of any FCC position shifts (§1.4).

Ideally, direct comparison of ground and on-orbit FCM measurements at as many lines as possible would provide a direct transfer of the absolute flux scale calibration from XRCF to orbit, or would provide direct measures of any discrepancies. In practise, some modelling is necessary due to possibly changing positions of the focal plane detector and the FCC relative to the HRMA, thermal contraction of the FCC on-orbit, and radioactive decay of the FCM sources. Finally, interpretation of any discrepancies with the HRMA model derived from the ground calibration requires ray trace simulations, for which we use the Project Science ray trace code (see Appendix A).

In the following subsections, we describe the characterization of the flight FCM radioactive sources (§1.2), the spectral analysis of FCM measurements taken at XRCF (§1.3), the registration analysis necessary to determine any positional shifts of the FCC relative to its nominal position (§1.4), and the continuing efforts to prepare for the FCM measurements to be taken during the activation phase after launch of the AXAF (§1.5).

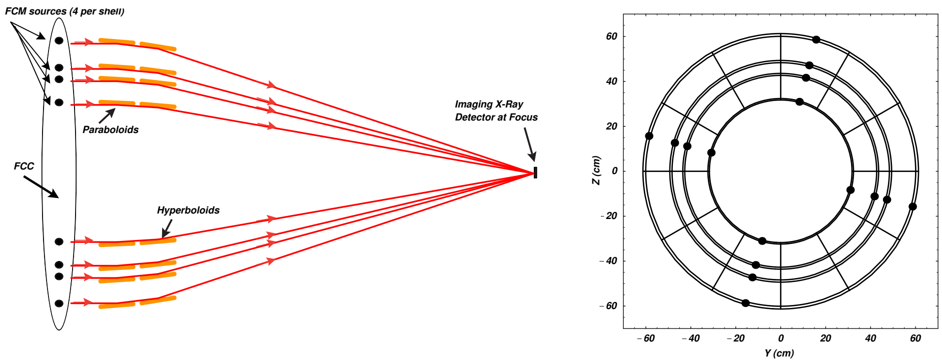

Figure 3: Left: The x-ray optical path for FCM measurements showing the FCM sources in the FCC, reflections of the paraboloids and hyperboloids of the four HRMA mirror shells, and collection by a focal plane detector (ACIS and, on the ground only, ACIS-2C and HRC-I). Right: Positions of the FCM sources projected on the paraboloid apertures midway between support struts for the baffle plates in the thermal pre-collimator, central aperture plate, and thermal post-collimator.

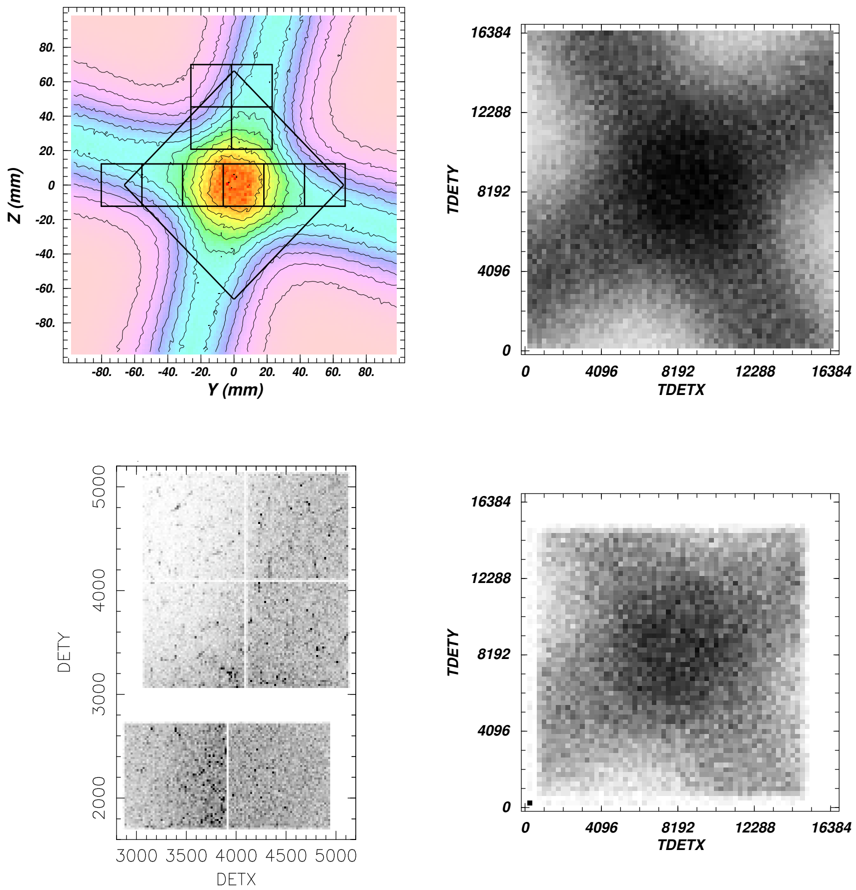

Figure 4: Simulated (top) and XRCF (bottom) FCM images. The simulated image in the top left shows the cross pattern generated in the focal plane by the FCM system, with outlines of the focal plane detectors ACIS and HRC-I superimposed. The image in the bottom left is a short ACIS exposure from XRCF. On the right are HRC-I images in HRC detector coordinates. On top is a simulation and on the bottom is an exposure from XRCF.

1.2 Radioactive sources

The FCM comprises sixteen (one per shell per quadrant) electron-capture sources positioned midway between baffle plate support struts (Fig. 3), containing ^{109}Cd and ^{55}Fe prepared at Isotope Products, Inc., packaged by MSFC, and mounted on the FCC. Due to leakage, MSFC sealed each source assembly with a 100-μm-thick Be window, eliminating the detectability and utility of the Mn Lα line at 0.64 keV. MSFC measured the individual FCM flight source activities (Table 1), with corroborating measurements by the US Army Redstone Arsenal. Dominated by systematic effects, the estimated errors in the measured absolute activities are ~15%. However, activity ratios between sources, dominated by statistical uncertainties, are known with significantly higher precision (< 1 %) than the absolute activities. Statistical uncertainties (1σ) in the ^{55}Fe activities, derived from measurements of the Mn Kα line strength, range from 0.2% (shell 1) to 0.4% (shell 6). Statistical uncertainties (1σ) in the ^{109}Cd activities, derived from measurements of the Ag Kα (22 keV) line strength, range from 0.04% (shell 1) to 0.1% (shell 6). However, the lower energy (~3 keV) lines in the Ag L series are significantly affected by the overlying material in the source assemblies. The internal configuration, from the substrate up, is ^{109}Cd (~0.3 μm), a gold buffer layer (~0.05 μm), ^{55}Fe (~0.1 μm), a gold sealing layer (~0.05 μm), and finally the beryllium window (100 μm). These layers absorb ~60% of the 3 keV Ag L series x-rays emitted from the ^{109}Cd. The range over which the actual layer thicknesses vary about their nominal values is unknown.

Ray trace simulations for the registration analysis (§ 1.4 below) use the activities given in Table 1. The radioactive half-lives of ^{109}Cd and ^{55}Fe are 1.2665±0.0011 and 2.73±0.03 yr [4], respectively, so compensation for radioactive decay is necessary in the data analysis.

MSFC also mapped source uniformities (Figs. 5, 6, 7 and 8). These uniformity maps are included in the ray trace simulations of the FCM sources. The uncertainty, which we assume is systematic, in the position of the uniformity map centers relative to the centers of the individual source buttons is ±0.2 mm in Y and Z. The tolerance on the position of the source buttons in the source holders is ±0.12 mm in Y and Z, while the tolerance on the position of the source holders on the FCC is ±0.08 mm in Y and Z. Assuming these tolerances are systematic errors, the systematic uncertainty in the position of the centers of the FCMs on the FCC is ±0.2 mm in Y and Z. Fig. 9 shows the measured PHA spectra for each shell 1 source, summed over its surface. PHA spectra for the other shells look very similar to these, but shifted down as the activities decrease for the inner shells.

Table 1: Nominal FCM source activities (mCi) on 1997 Mar 5* and radii (mm).

Shell	-15	75	165	255	Average	**Source radius**
1	(4.03,1.20)	(3.53,0.84)	(4.03,0.93)	(3.61,0.84)	(3.8,0.95)	4.500
3	(2.44,0.73)	(2.21,0.79)	(2.44,0.79)	(2.12,0.85)	(2.3,0.79)	3.625
4	(1.56,0.47)	(1.49,0.47)	(1.56,0.48)	(1.40,0.51)	(1.5,0.48)	3.200
6	(0.78,0.26)	(0.61,0.24)	(0.73,0.24)	(0.61,0.23)	(0.68,0.24)	2.380

* The first number is for ^{109}Cd and the second for ^{55}Fe.

MSFC used Monte-Carlo simulation of the source assemblies to determine fluxes in the forward direction. Predicted absolute fluxes for electron-capture lines are no more accurate than the absolute activity measurements, but relative fluxes should be as accurate as the tabulated branching ratios - a few % [4]. Predicted fluxes, absolute or relative, for fluorescent lines produced in the assemblies (primarily by the Ag Kα line at 22 keV) are much less secure due to the complexity of the simulations and the number of interaction pathways.

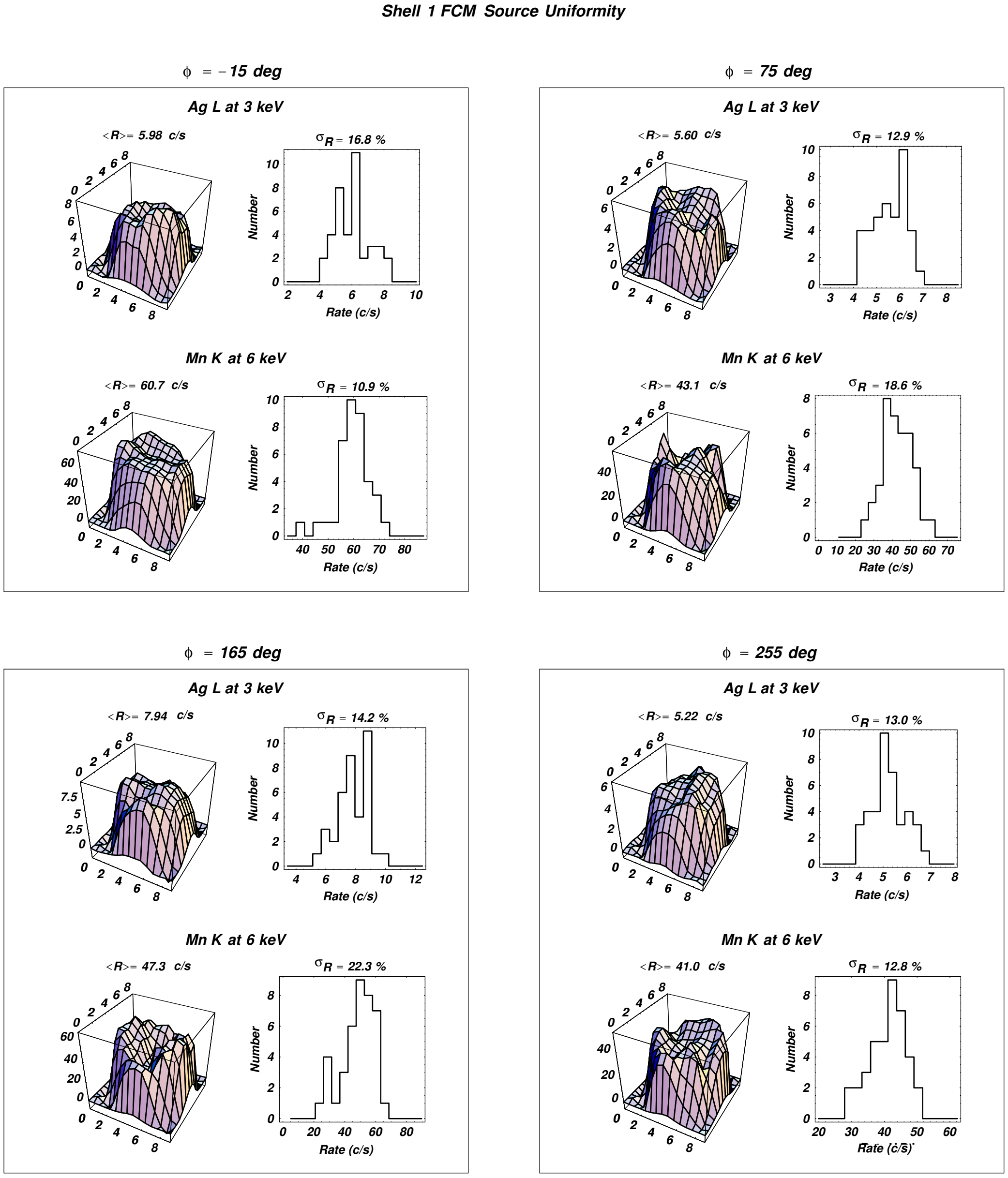

Figure 5: Uniformity measurements for the shell 1 FCM sources at each of the 4 azimuths. Within each panel are uniformity results at 3 keV (top, ^{109}Cd source) and 6 keV (bottom, ^{55}Fe source). At each energy are a surface plot of rate (left, and a histogram of rates (right). $< R >$ is the mean rate in c/s and σ_R is the rms dispersion about $< R >$ in %. These measurements were made with a CZT detector and a 1-mm-diameter pinhole.

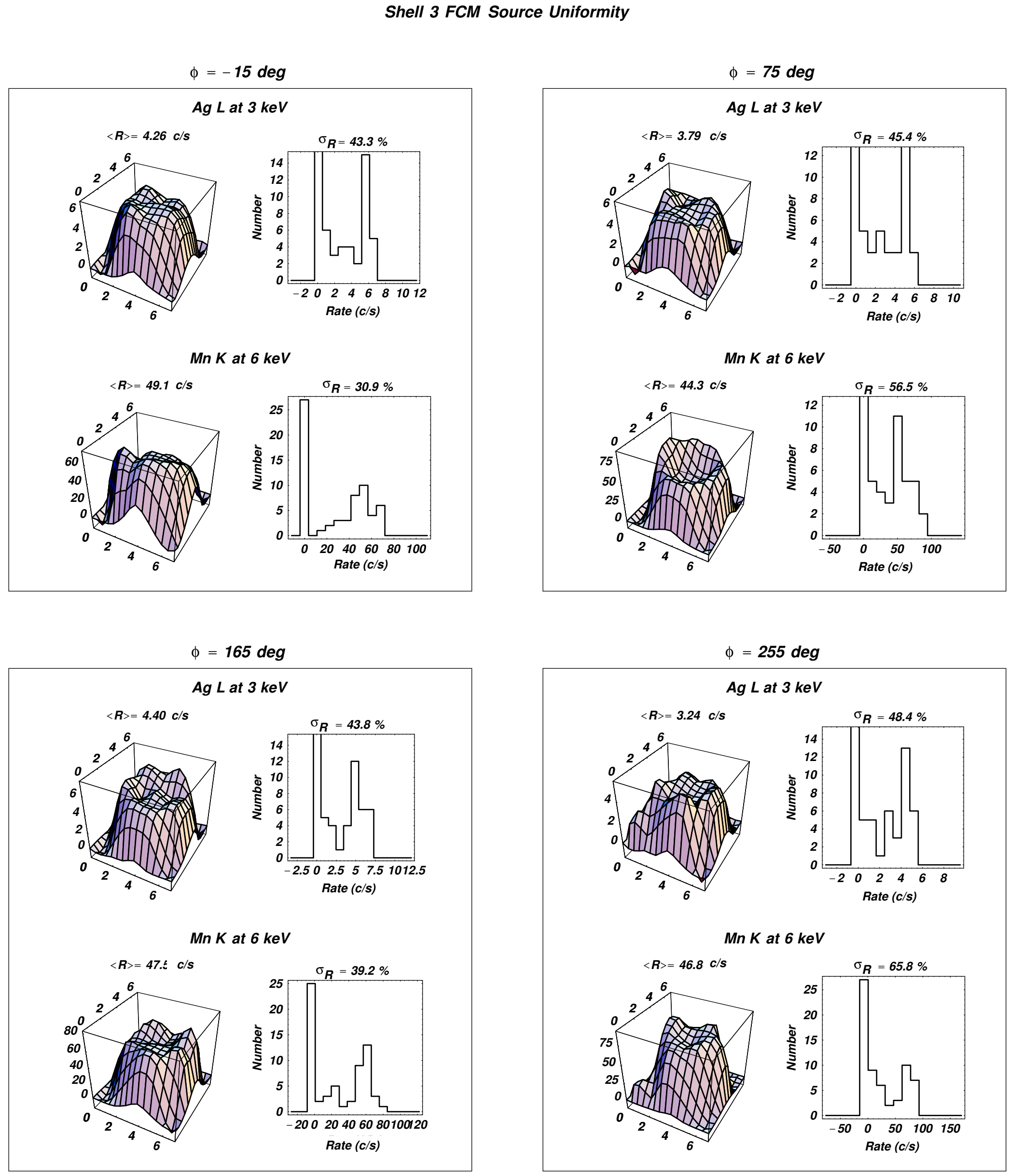

Figure 6: Uniformity measurements for the shell 3 FCM sources at each of the 4 azimuths. Within each panel are uniformity results at 3 keV (top, ^{109}Cd source) and 6 keV (bottom, ^{55}Fe source). At each energy are a surface plot of rate (left, and a histogram of rates (right). $< R >$ is the mean rate in c/s and σ_R is the rms dispersion about $< R >$ in %. These measurements were made with a CZT detector and a 1 mm diameter pinhole.

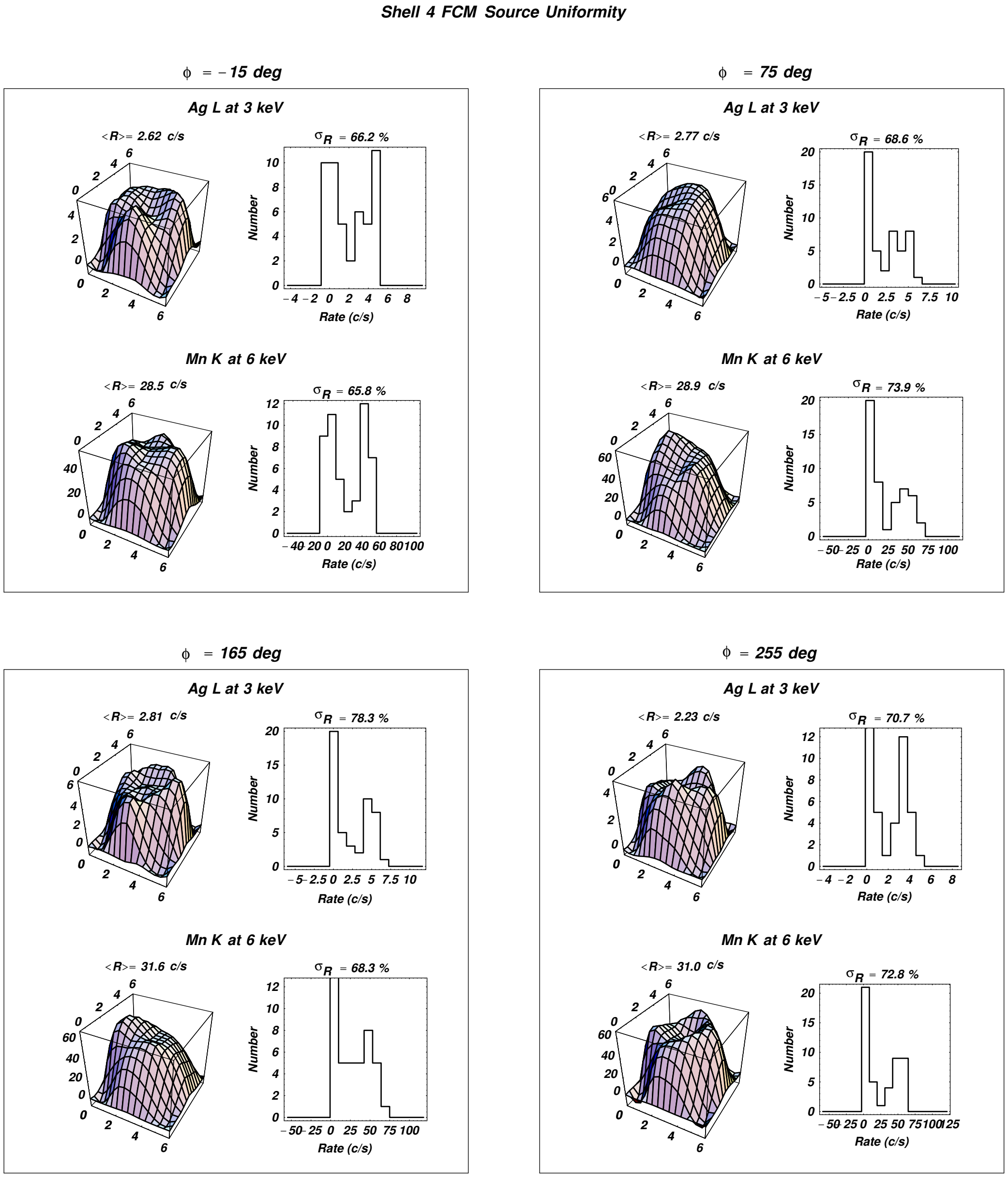

Figure 7: Uniformity measurements for the shell 4 FCM sources at each of the 4 azimuths. Within each panel are uniformity results at 3 keV (top, ^{109}Cd source) and 6 keV (bottom, ^{55}Fe source). At each energy are a surface plot of rate (left, and a histogram of rates (right). $< R >$ is the mean rate in c/s and σ_R is the rms dispersion about $< R >$ in %. These measurements were made with a CZT detector and a 1 mm diameter pinhole.

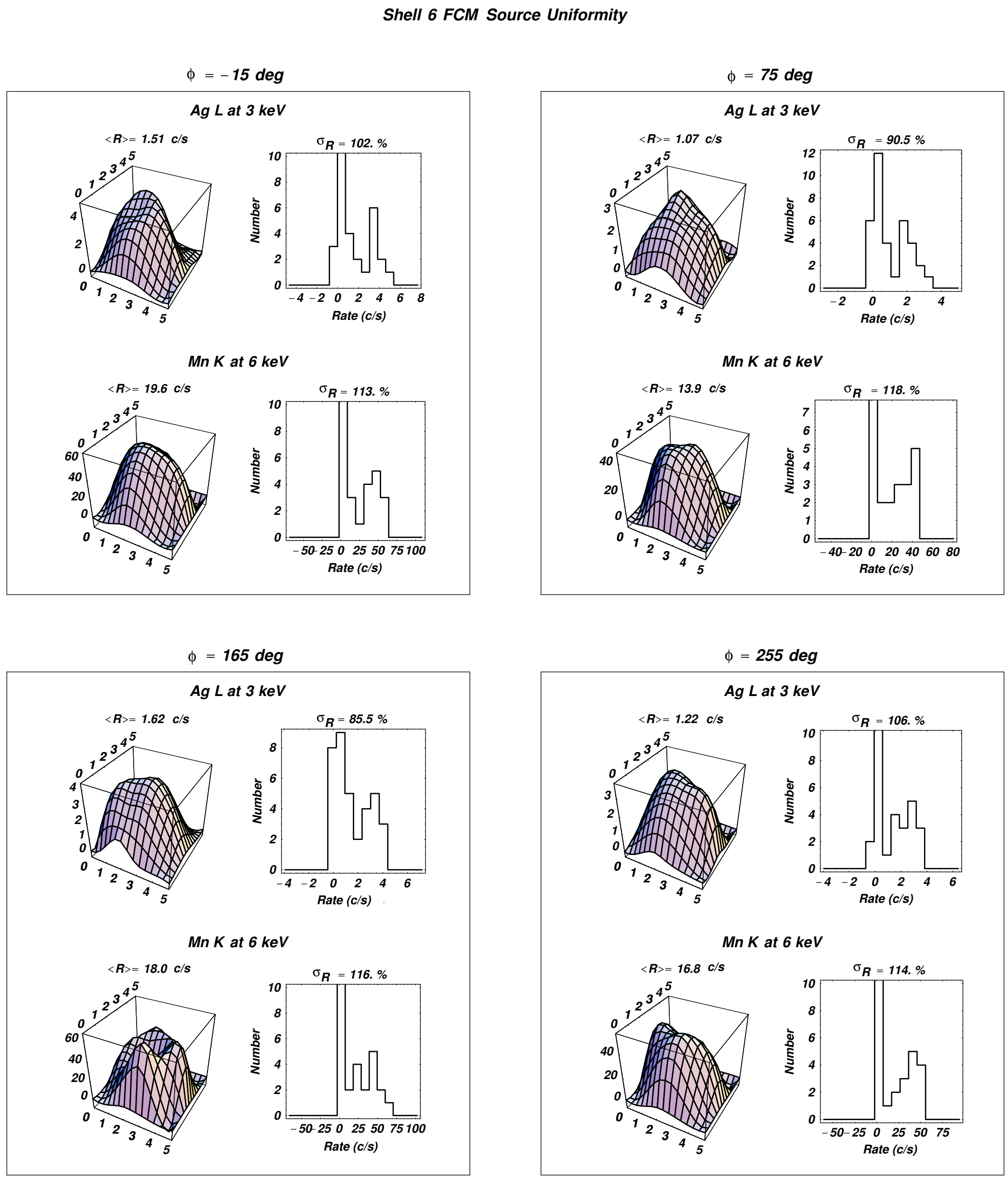

Figure 8: Uniformity measurements for the shell 6 FCM sources at each of the 4 azimuths. Within each panel are uniformity results at 3 keV (top, ^{109}Cd source) and 6 keV (bottom, ^{55}Fe source). At each energy are a surface plot of rate (left, and a histogram of rates (right). $< R >$ is the mean rate in c/s and σ_R is the rms dispersion about $< R >$ in %. These measurements were made with a CZT detector and a 1 mm diameter pinhole.

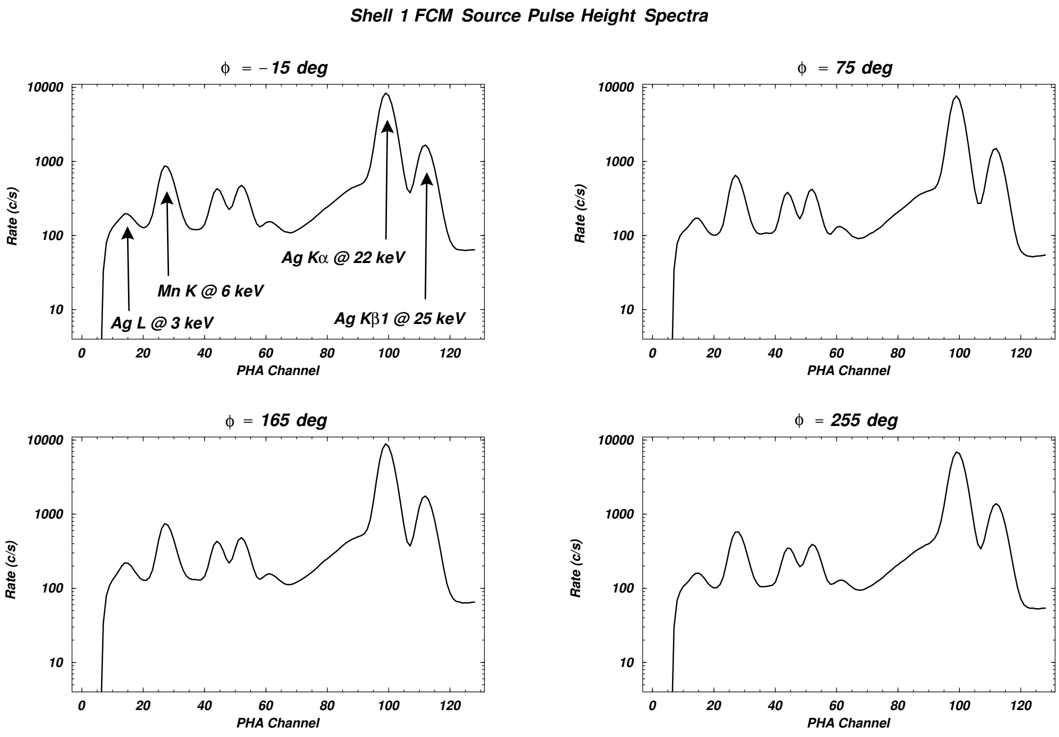

Figure 9: PHA spectra, summed over the source, for the shell 1 FCM sources at each of the 4 azimuths. The prominent Ag K lines at 22 and 25 keV do not reflect from the HRMA and so are not detected by ACIS. PHA spectra for the other shells are very similar, but shifted down as the activities decrease for the inner shells.

1.3 Spectral analysis

So far analysis of FCM data has focused almost exclusively on one data set (TRW ID H-IAS-RC-1.001), which has by far the most data (12,900 s of good time), and was taken with the ACIS detector at a position along the optical axis closest to the expected on-orbit position (∼190 mm in front of the finite conjugate focus at XRCF). The position of the optical axis in ACIS detector coordinates was placed near the nominal position for the S array (Fig. 10), and was determined *a posteriori* from an appropriate ACIS boresight position provided by the ACIS team and from the Five Axis Mount (FAM) logs to be (DETX = 4148 pixels, DETY = 2214 pixels). DETX is in the dispersion direction (Y) and DETY is in the SIM motion direction (Z). This position is accurate to within an estimated 10 pixels which we believe is sufficient for purposes of FCM analysis. The six readout CCDs were all four I array front-side-illuminated CCDs and the two S array CCDs S2 (front-side-illuminated) and S3 (back-side-illuminated).

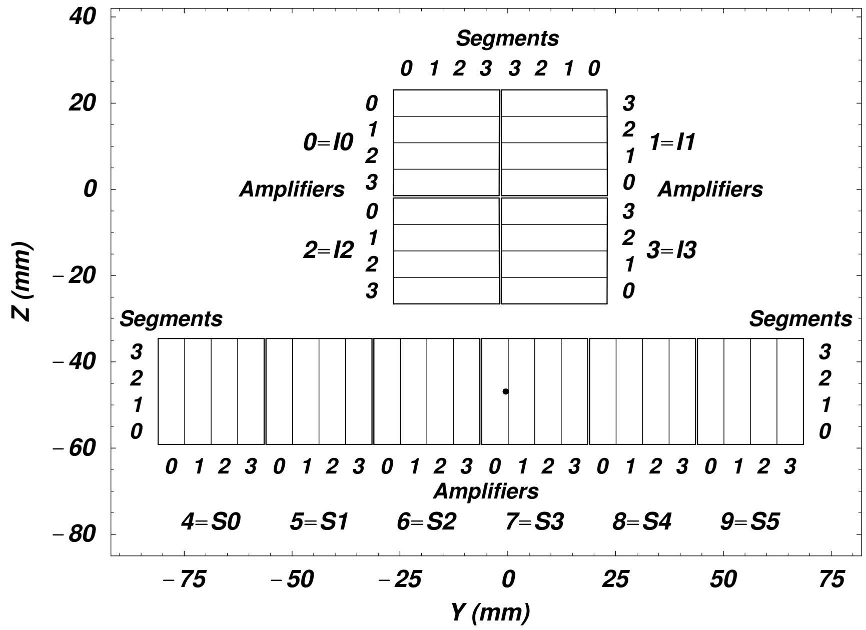

Figure 10: ACIS detector layout showing CCD, amplifier, and segment identifiers. The amplifiers are read out individually, and run horizontally for the I array CCDs and vertically for the S array CCDs. For the spectral and FCC position registration analysis, each amplifier was divided into 4 segments. Also shown by the black dot in amplifier 0 of CCD S3 is the position of the optical axis for the XRCF FCM measurement described in this paper.

ASCA grades 0, 2, 3, 4 and 6 were selected for further analysis. Using resolution curves appropriate for the front-side- and back-side-illuminated CCDS, the spectral content of the detected counts was determined by fitting gaussian lines to the line list [5] given in Table 2 using the following PLT/COD function:

```
! P1,P2 gain offset slope
! P3,P4 resolution parameters
! P5    tail
! Line energies:
VAR eSiKa    1739.8 eSiKa   STO
VAR eSiKb    1835.9 eSiKb   STO
VAR eAuMa    2121.3 eAuMa   STO
VAR eAuMb    2205.0 eAuMb   STO
```

```
VAR eAgLl    2633.7 eAgLl   STO
VAR eAgLn    2806.1 eAgLn   STO
VAR eAgLa    2982.3 eAgLa   STO
VAR eAgLb1   3150.9 eAgLb1  STO
VAR eAgLb4   3203.5 eAgLb4  STO
VAR eAgLb3   3234.5 eAgLb3  STO
VAR eAgLb6   3256.0 eAgLb6  STO
VAR eAgLb2   3347.8 eAgLb2  STO
VAR eAgLg1   3522.6 eAgLg1  STO
VAR eAgLg2   3743.2 eAgLg2  STO
VAR eMnKa    5895.1 eMnKa   STO
VAR eFeKa    6400.0 eFeKa   STO
VAR eMnKb1   6490.4 eMnKb1  STO
VAR eNiKa    7472.4 eNiKa   STO
VAR eCuKa    8041.1 eCuKa   STO
VAR eAuLl    8493.9 eAuLl   STO
VAR eAuLa    9713.0 eAuLa   STO
VAR eSiKEd   1840.0 eSiKEd  STO
! General variable
var Energy
var Shelf
!*************************************************************************
! Subroutines:
! push channel on stack, return the Energy
! Assumes E=p1+chan*p2
: gain
p2 * p1 + DUP eSiKEd RCL < IF
P31 -
THEN
;
!*************
! Returns gaussian, push norm, width, energy onto stack
: ngaus
DUP Energy RCL > IF
3 PICK P5 * Shelf RCL + Shelf STO
THEN
Energy RCL - over / dup * 2 / neg exp swap / * 2.50663 / P2 *
;
!*************
! Assume Energy is on stack, return SSD resolution
! Uses sigma = SQRT(P4*E+P3)
: ssdres  P4 * P3 + SQRT ;
!*************************************************************************
: calsp
x gain Energy STO
0.0 Shelf STO
0.0
 P6  eSiKa   RCL DUP ssdres SWAP ngaus +
 P7  eAuMa   RCL DUP ssdres SWAP ngaus +
 P8  eAuMb   RCL DUP ssdres SWAP ngaus +
 P9  eAgLl   RCL DUP ssdres SWAP ngaus +
 P10 eAgLn   RCL DUP ssdres SWAP ngaus +
 P11 eAgLa   RCL DUP ssdres SWAP ngaus +
 P12 eAgLb1  RCL DUP ssdres SWAP ngaus +
```

```
 P13 eAgLb4  RCL DUP ssdres SWAP ngaus +
 P14 eAgLb3  RCL DUP ssdres SWAP ngaus +
 P15 eAgLb6  RCL DUP ssdres SWAP ngaus +
 P16 eAgLb2  RCL DUP ssdres SWAP ngaus +
 P17 eAgLg1  RCL DUP ssdres SWAP ngaus +
 P18 eAgLg2  RCL DUP ssdres SWAP ngaus +
 P19 eMnKa   RCL DUP ssdres SWAP ngaus +
 P20 eFeKa   RCL DUP ssdres SWAP ngaus +
 P21 eMnKb1  RCL DUP ssdres SWAP ngaus +
 P22 eAuLa   RCL DUP ssdres SWAP ngaus +
 P23 eNiKa   RCL DUP ssdres SWAP ngaus +
 P24 eCuKa   RCL DUP ssdres SWAP ngaus +
 P25 eAuLl   RCL DUP ssdres SWAP ngaus +
! Escapes
 P26 eAgLa   RCL eSiKa RCL - DUP ssdres SWAP ngaus +
 P27 eAgLb1  RCL eSiKa RCL - DUP ssdres SWAP ngaus +
 P28 eMnKa   RCL eSiKa RCl - DUP ssdres SWAP ngaus +
! Line at specified energy
P30  P29         DUP ssdres SWAP ngaus +
Shelf RCL +
;
```

Fits were first carried out for each amplifier on each of the six readout CCDs (Fig. 10). Holding line widths frozen at their best fit values for each amplifier, fits were then carried out for each segment in order to determine rates in each line. The 96 data points per line resulting from this procedure are sufficient for determining FCC position shifts. Figure §11 shows the fitted spectra for a selected segment on the front-side-illuminated CCD I3 and one on the back-side-illuminated CCD S3. These segments lie near one another and above the optical axis (Fig. 10). The strongest lines in these spectra are the electron-capture lines Ag Lα, the Ag Lβ series, Mn Kα, and Mn Kβ1. The superior energy resolution of the front-side-illuminated CCDs is apparent. Appendix B lists fitted rates for Ag Lα, the sum over the Ag Lβ series, Mn Kα, and Mn Kβ1 in each segment, amplifier and CCD. Comparison of these XRCF line rates with those measured on orbit, corrected for radioactive decay and FCC position shifts, comprises the verification of the AXAF absolute flux calibration transfer and provides the basis for the search for any possible changes in molecular contamination.

Table 2: Line list for spectral fits.

Line	Energy (keV)	Line	Energy (keV)
Si K escape peak for Ag Lα	1.2425	Ag Lγ1	3.5226
Si K escape peak for Ag Lβ1	1.4111	Ag Lγ2	3.7432
Si Kα	1.7398	Si K escape peak for Mn Kα	4.1553
Au Mα	2.1213	Mn Kα	5.8951
Au Mβ	2.2050	Fe Kα	6.4000
Ag Lℓ	2.6637	Mn Kβ1	6.4904
Ag Lη	2.8061	Ni Kα	7.4724
Ag Lα	2.9823	Cu Kα	8.0411
Ag Lβ1	3.1509	Au Lℓ	8.4939
Ag Lβ6	3.2560	Au Lα	9.7130
Ag Lβ2	3.3478		

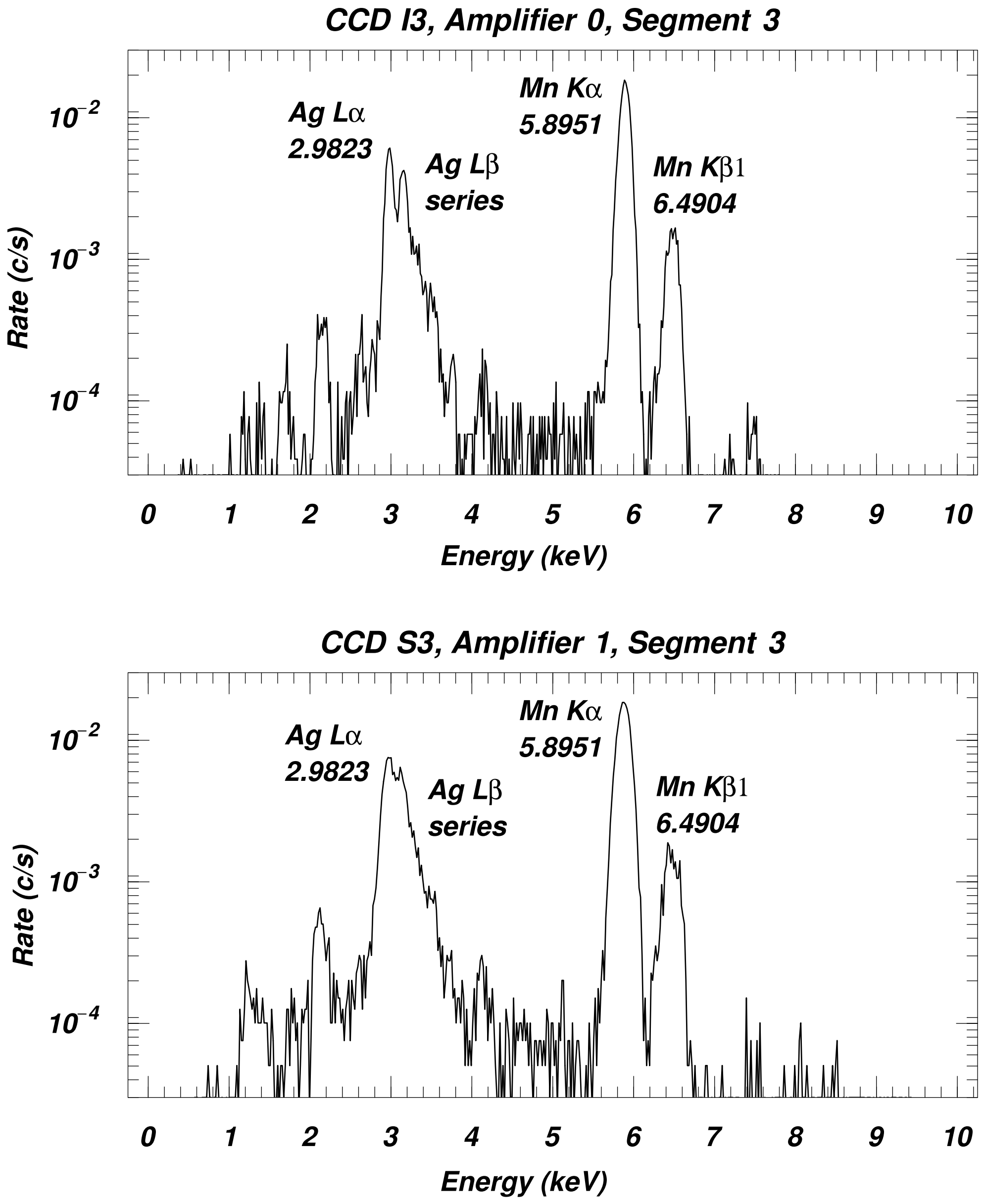

Figure 11: FCM/HRMA/ACIS spectra for a selected segment on the front-side-illuminated CCD I3 (top), and one on the back-side-illuminated CCD S3 (bottom).

1.4 FCM registration analysis

Because the on-orbit positions of the FCM sources relative to the optical axis will change with respect to their XRCF positions due to thermal contraction of the FCC about an off-axis fixed point, as well as launch vibrations, it is necessary to register the FCM images at XRCF and on-orbit by comparing them to simulated images, and to search for positional shifts of the axis of the FCC relative to the optical axis. Eastman-Kodak measured FCM source positions on the FCC with respect to its nominal axis [6]. During XRCF testing, the FCC V-groove-block and cup-cone positioning mechanism was not aligned, and the magnitude of the resulting displacement, while visually estimated at <1 mm mostly in Z, is not known accurately. Simulated images for cross-correlation with the data are generated using the ray trace code written by MSFC Project Science, described in Appendix A, with the as-built HRMA mirror parameters and mirror figure deviations provided by the AXAF Mission Support Team [7]. Table 3 lists the expected displacements of the FCM sources from the centers of the paraboloid apertures assuming the nominal FCC axis was aligned with the optical axis of the P3 mirror. The systematic error in these nominal positions is ± 0.2 mm in Y and Z (see §1.2). If these numbers correctly represented reality, the registration procedure should find little if any FCC displacement (*i.e.* $\Delta \mathrm{Y} \simeq \Delta \mathrm{Z} \simeq 0$). FCM source non-uniformity (§1.2) is included in the ray trace. Nominally the centers of the uniformity maps lie on the centers of the FCM sources; however, there is a systematic uncertainty of ± 0.2 mm in Y and Z in the relative positions of these points.

Table 3: Expected FCM displacements (mm) from centers of paraboloid apertures*.

Shell/Azimuth	-15	75	165	255
1	(0.258,-0.051)	(-0.087,-0.159)	(-0.151,0.059)	(-0.180,-0.505)
3	(0.221,-0.059)	(-0.061,-0.228)	(-0.078,0.021)	(-0.135,-0.505)
4	(0.213,-0.030)	(-0.066,-0.219)	(-0.077,0.048)	(-0.134,-0.475)
6	(0.092,-0.005)	(-0.069,-0.240)	(-0.227,-0.042)	(-0.137,-0.495)

* Assuming the nominal FCC axis aligned with the the optical axis of mirror P3. The first number is for Y and the second for Z.

The ACIS flat fields at Nb Lα (E = 2.165 keV) and Fe Kα (E = 6.400 keV) are very flat (< 1% variations) when all grades are accepted. However, for the back-side-illuminated CCD S3, accepting only ASCA grades 0, 2, 3, 4 and 6, and applying a spectral analysis similar to that described in §1.3, these flat fields do show noticeable variations. For S3, the variation is about 8% and 19% at 2.165 and 6.400 keV, respectively, with the highest response closest to and the lowest response furthest from the readout (Table 4). For the correlation analysis we correct the S3 rates derived from the spectral analysis (§1.3) for this flat field effect by interpolating linearly in energy (Tables 5 and 6). A further small complication, not yet included in the analysis, is the slight difference in vignetting of the first few rows due to frame store shielding for the flat field and FCM measurements. At present, we carry out the cross-correlation registration analysis at the strongest lines, Ag Lα and Mn Kα (E = 2.982 and 5.895 keV, respectively), letting the overall normalization and the relative efficiencies between front-side- and back-side-illuminated CCDs assume values that minimize the value of χ^2 at the various trial positions of the FCC. We also carry out the analysis at the rate weighted average energy of the Ag Lβ series (E = 3.198) and at Mn Kβ1 (E = 6.490 keV).

Although the ray-trace images generated using the Project Science ray trace code appear to adequately reproduce the XRCF images (Fig. 12), in fact the results given in Table 7 show that the best-fits are statistically unacceptable. The left-hand side of Fig. 13 shows error contours established by rescaling χ^2 values to 1 per degree of freedom at the best-fit [8] assuming the nominal positions of the FCM on the FCC and perfect alignment of the uniformity map and FCM centers. For this case the FCC position shift derived at Mn Kα does not agree within the assigned errors with that derived at Ag Lα or at the Ag Lβ series, although the Ag L results are in agreement with each other. Obviously the FCC position shift should not depend on energy.

Possible explanations for this disagreement include, but are not limited to, shifts within tolerances of the FCM positions away from their nominal values on the FCC, and misalignment within tolerances of the uniformity map centers with the FCM centers. It is possible to bring the Mn Kα FCC position shift into better agreement with the Ag L results by appealing to these tolerances, although the fits are still statistically unacceptable. The right-hand side of Fig. 13 shows errors contours calculated as before but assuming:

1. All shell 1 FCM sources are shifted from their nominal positions on the FCC by -0.1 mm in Y and +0.2 mm in Z.
2. All shell 3, 4, and 6 FCM sources are shifted from their nominal positions on the FCC by +0.1 mm in Y and -0.2 mm in Z.
3. All shell 1 uniformity map centers are shifted from their nominal positions relative to the FCM centers by +0.1 mm in Y and -0.2 mm in Z.
4. All shell 3, 4, and 6 uniformity map centers are shifted from their nominal positions relative to the FCM centers by -0.1 mm in Y and +0.2 mm in Z.

The chosen shifts in Z are at the extreme limits of the tolerances. Table 7 lists the registration results for the nominal case and for the case with the shifts described above. Also given are mean values weighted by the assigned errors. Projections of the FCM sources onto the paraboloid apertures shows that these results imply a slight vignetting of the shell 6 source at an azimuth of 75 deg (Fig. 14). The individual FCM sources are securely mounted in the FCC so that we do not expect any change after launch in their relative positions except that due to a slight thermal contraction of the FCC on-orbit.

Table 4: Fitted flat field corrections (ASCA grades 0, 2, 3, 4 and 6), normalized to an average value of unity, for the back-side-illuminated CCD S3 at Nb Lα (E = 2.165 keV) and Fe Kα (E = 6.400 keV).

segment	0	1	2	3	segment	0	1	2	3
amplifier	E = 2.165 keV				amplifier	E = 6.400 keV			
0	1.004	1.008	1.000	0.949	0	1.083	1.052	0.989	0.889
1	1.008	1.024	1.000	0.993	1	1.073	1.058	1.000	0.926
2	0.997	1.028	1.012	0.997	2	1.068	1.047	1.005	0.926
3	1.008	1.012	0.997	0.961	3	1.047	1.010	0.937	0.889

Table 5: Interpolated flat field corrections (ASCA grades 0, 2, 3, 4 and 6) for the back-side-illuminated CCD S3 at Ag Lα (E = 2.982 keV) and the rate weight mean energy for the Ag Lβ series (E = 3.198 keV).

segment	0	1	2	3	segment	0	1	2	3
amplifier	E = 2.982 keV				amplifier	E = 3.198 keV			
0	1.020	1.017	0.998	0.938	0	1.024	1.019	0.998	0.935
1	1.021	1.031	1.000	0.980	1	1.024	1.032	1.000	0.976
2	1.010	1.032	1.011	0.983	2	1.014	1.033	1.010	0.979
3	1.016	1.012	0.985	0.947	3	1.018	1.012	0.982	0.944

Table 6: Interpolated flat field corrections (ASCA grades 0, 2, 3, 4 and 6) for the back-side-illuminated CCD S3 at Mn Kα (E = 5.895 keV) and Mn Kβ1 (E = 6.490 keV).

segment	0	1	2	3	segment	0	1	2	3
amplifier	E = 5.895 keV				amplifier	E = 6.490 keV			
0	1.074	1.047	0.991	0.896	0	1.086	1.053	0.989	0.888
1	1.066	1.054	1.000	0.934	1	1.075	1.058	1.000	0.925
2	1.060	1.045	1.006	0.934	2	1.070	1.047	1.005	0.925
3	1.042	1.010	0.944	0.898	3	1.048	1.010	0.935	0.888

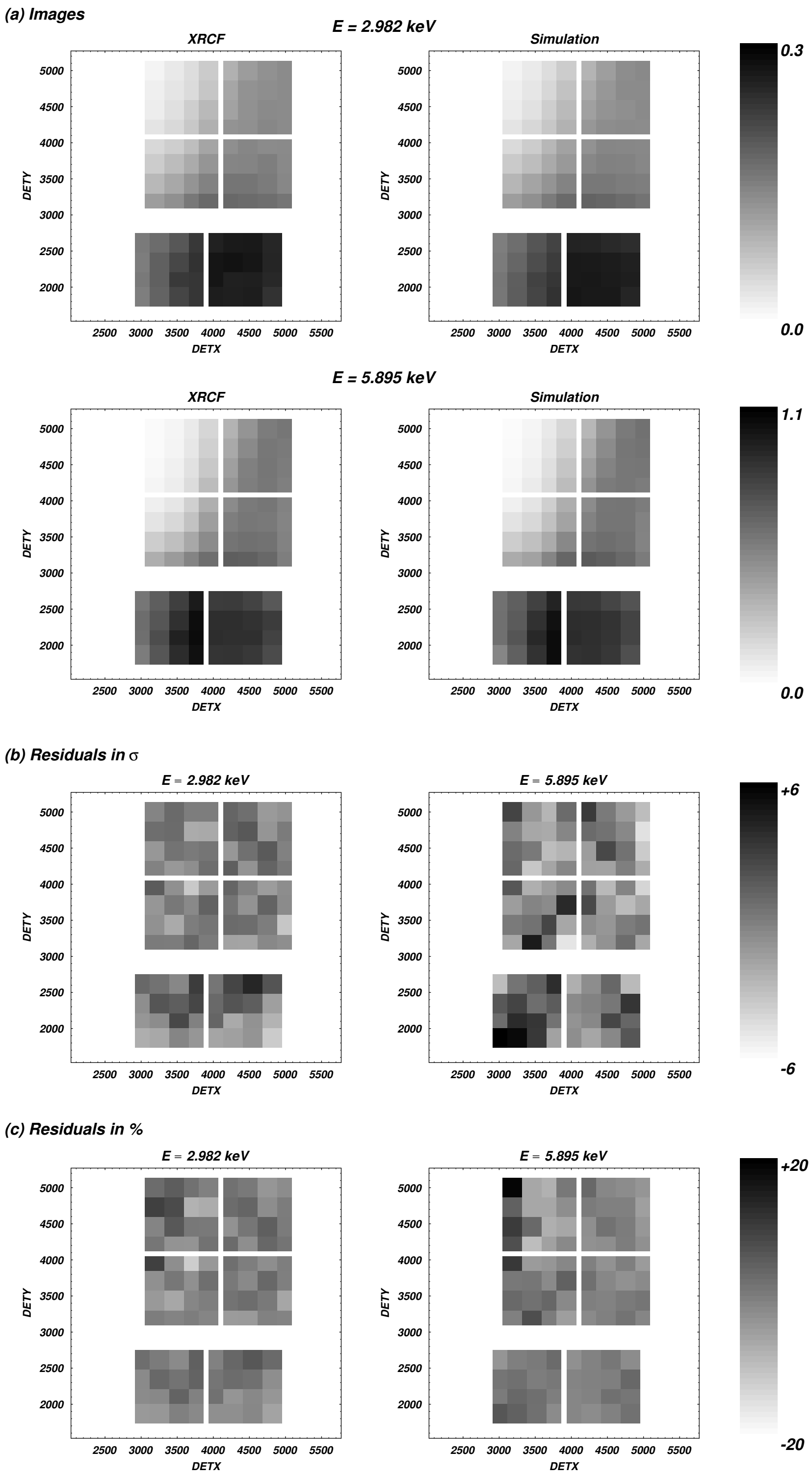

Figure 12: FCC registration results at 2.982 keV and 5.895 keV, for FCM located at their nominal positions on the FCC and for perfect alignment of the uniformity map centers. (a) XRCF images are shown on the left and the best-fit ray-trace images on the right. (b) Residuals in sigma. (c) Residuals in percent.

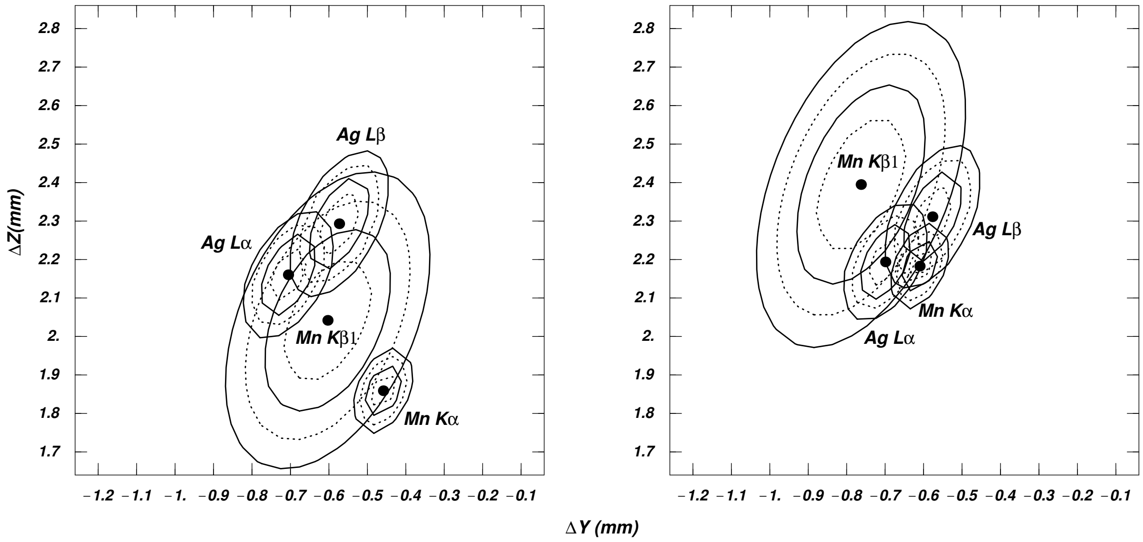

Figure 13: Best-fit values for ΔY and ΔZ and error contours derived by rescaling χ^2 so that $\chi^2_{min} = 94$ and setting $\chi^2 = \chi^2_{min} + \Delta\chi^2$ with $\Delta\chi^2 = 1$, 2.30, 4, and 6.17. Extremes on the $\Delta\chi^2 = 1$ and 4 contours determine the 1σ and 2 σ single parameter errors, while the $\Delta\chi^2 = 2.30$ and 6.17 contours enclose the 68.3% and 95.4% two parameter confidence levels. Left: Results for nominal positions of the FCM on the FCC and for perfect alignment of the FCM and uniformity map centers. Right: Results for a particular choice (see text) of FCM positions shifts on the FCC and misaligned uniformity map centers. The chosen shifts in Z are at the extreme limit of the tolerances.

Table 7: Present status of registration analysis. The values of ΔY and ΔZ are shifts of the FCC center from its nominal position at Y = 0 and Z = 0.

	Nominal				With shifts			
Energy (keV)	χ^2_{min} *	**ΔY**† **(mm)**	**ΔZ**† **(mm)**	**Corr.**	χ^2_{min} *	**ΔY**† **(mm)**	**ΔZ**† **(mm)**	**Corr.**
2.982	201.5	-0.706±0.041	2.160±0.058	0.52	183.9	-0.699±0.038	2.194±0.053	0.53
3.198	242.2	-0.573±0.044	2.293±0.065	0.48	246.5	-0.577±0.043	2.311±0.064	0.49
5.895	455.2	-0.459±0.029	1.859±0.040	0.70	439.5	-0.610±0.028	2.183±0.040	0.66
6.490	452.5	-0.603±0.097	2.042±0.140	0.59	457.4	-0.763±0.098	2.395±0.150	0.55
Weighted means		-0.550±0.020	2.025±0.029			-0.633±0.020	2.217±0.028	

* These fits are statistically unacceptable.

† Errors are standard (1σ, 1 parameter) errors based on rescaling χ^2_{min} to 1 per degree of freedom.

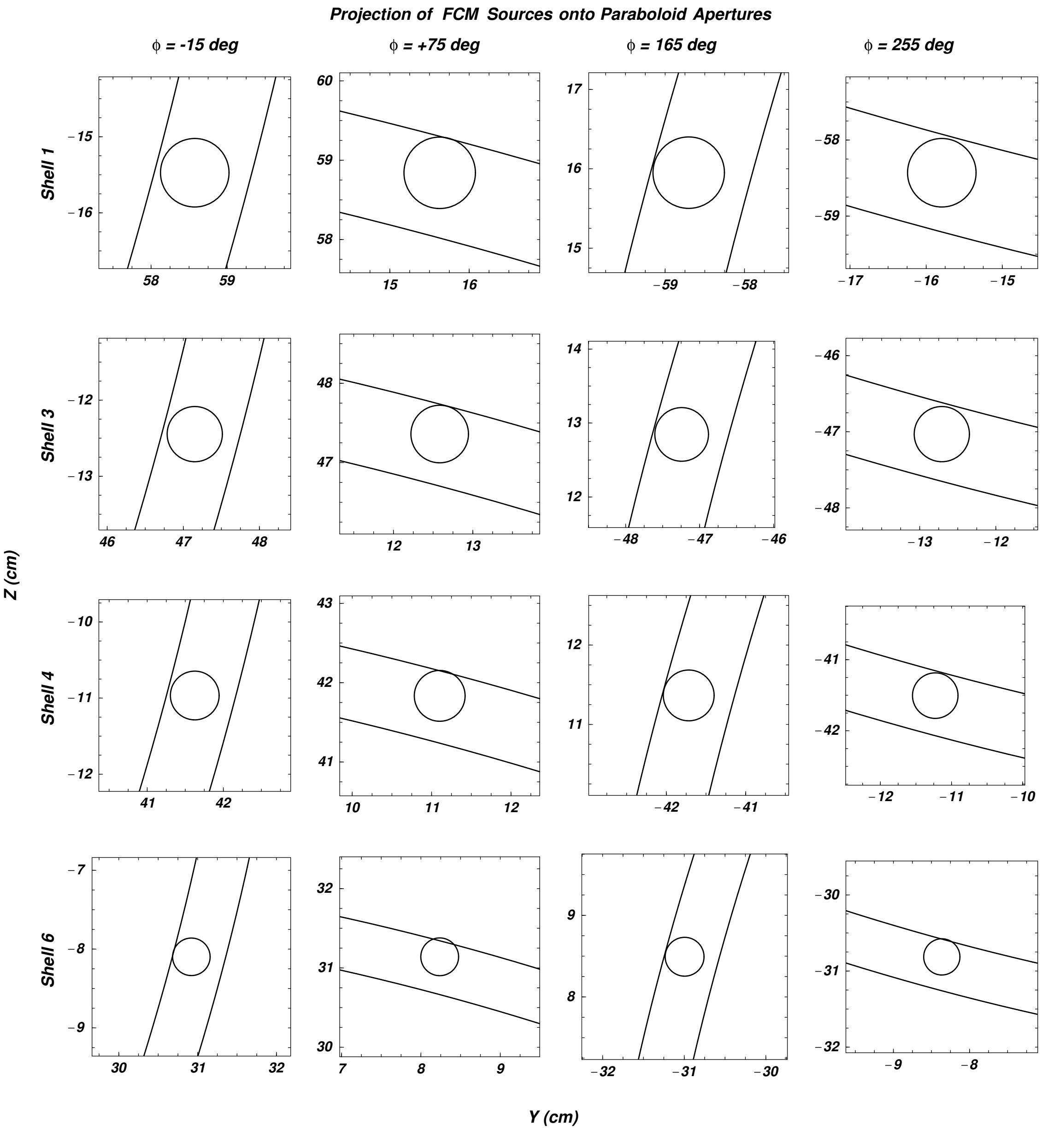

Figure 14: Projections of the FCM sources, including FCC displacement from its nominal position using ΔY = -0.633 mm and ΔZ = +2.217 mm (see the case with shifts in Table 7), onto the aperture of the paraboloids. For shell 6, there is a slight vignetting of the source at an azimuth of 75 deg.

1.5 Future Work

After launch the present plan is for a 30,000 s measurement with the four I array CCDs plus S2 and S3 and a 30,000 s measurement with the six S array CCDs. For both measurements, the ACIS detector will be in its launch-lock position with the optical axis in S3, same as for the XRCF measurement described here. We will:

1. Analyze the on-orbit FCM/HRMA/ACIS data in a manner consistent with the analysis presented here.
2. Register images at as many energies as possible, taking into account thermal contraction of the FCC (Table 8).
3. Compare the on-orbit rates with XRCF rates and model predictions, including the effects of FCC position shifts and FCM source decay.
4. Resolve discrepancies.

Table 8: Expected changes in source ΔY, ΔZ and ΔR, in mm, due to on-orbit thermal contraction about the fixed point Y = 0.9525 cm and Z = 65.438 cm, assuming a temperature change from ground (at XRCF) to orbit of -32 F. The values tabulated here change only slightly if alignment shifts slightly change the position of the fixed point.

ϕ	-15°			75°			165°			255°		
S	ΔY	ΔZ	ΔR	ΔY	ΔZ	ΔR	ΔY	ΔZ	ΔR	ΔY	ΔZ	ΔR
1	-.240	+.338	-.319	-.061	+.028	+.012	+.248	+.207	-.186	+.069	+.516	-.517
3	-.192	+.325	-.270	-.049	+.076	+.061	+.200	+.220	-.137	+.057	+.469	-.467
4	-.169	+.319	-.246	-.042	+.099	+.085	+.177	+.226	-.113	+.050	+.446	-.444
6	-.125	+.307	-.200	-.031	+.144	+.131	+.133	+.238	-.067	+.039	+.401	-.398

Finally, we will work with the AXAF Mission Support Team and the AXAF Science Center to interpret results with respect to absolute flux calibration and to implications for HRMA modelling (*e.g.*, changes in molecular contamination). We hope and expect that there will be none.

A Project Science ray-trace code

A.1 Purpose

Long, long ago, in a galaxy far, far away,....

Before the VETA-1 test, Project Science decided that it was worthwhile to develop its own ray trace code for the following reasons:

1. To have its own tool for understanding the design of the HRMA, and the effect of design changes.
2. To have an independent code as a check on the codes maintained by the Mission Support Team (MST) and others.

The Project Science ray trace code does not have all the features of the high-fidelity code maintained by the Mission Support Team, but it permits reasonably rapid response when new studies are needed. Most often work can proceed without requests for ray files generated by the MST. It has proven useful in studies of coating materials for the HRMA, the effects of coating properties such as density and density gradients on HRMA throughput, comparison of effective area measurements and predictions, and studies of the FCM system both for design and for predictions to fit to FCM data. While algorithm development was carried out in *Mathematica*$^{\rm TM}$, the code is in FORTRAN and runs on a SGI ORIGIN computer at MSFC. The code uses the as-built HRMA parameters and mirror figure deviations provided by the AXAF MST [7] (we especially thank Leon Van Speybroeck, Terry Gaetz, Ping Zhao, and Diab Jerius for providing these data and for helpful discussions). The Project Science ray trace code reproduces the effective areas predicted by the MST code [9]. It also reproduces the XRCF focal lengths for individual mirror shells given in the MST preliminary report on HRMA calibration results [7]. The Project Science code predicts on-orbit focal lengths for the four mirror shells that are $\sim 100\mu$m longer than those predicted by MST. This is most probably due to differing methods used for figure error interpolation (MST uses spline interpolation while Project Science uses simple linear interpolation), and the resulting differences in mean grazing angle adjustments. Here we briefly describe the Project Science ray trace code and what it can and cannot do.

A.2 Geometric ray trace

The Project Science ray trace code is primarily a tool for the geometric tracing of rays through a Wolter Type-I paraboloid-hyperboloid x-ray telescope. The main body of the code divides into:

1. Setup.
2. Ray initiation according to chosen source properties.
3. Propagation through the thermal pre-collimator.
4. Propagation through the paraboloid.
5. Propagation through the central aperture plate.
6. Propagation through the hyperboloid.
7. Propagation to a nominal focal plane.
8. Record ray position, direction, and reflection grazing angles to a file.
9. Record summary of run upon completion.

Various tasks are carried out in post-processing programs which we describe in §A.4.

A.2.1 Setup

As one might expect, the setup section of the code defines various constants, sets up arrays, asks the user what type of simulation he wants to run (which shell; with or without figure errors; with or without baffling; number of rays; source type; etc.), and calls subroutines to set the mirror shell and other telescope parameters.

A.2.2 Ray initiation

The initial position and direction of a ray is set according to the type of source chosen by the user. For a point source on the sky, the rays are uniformly distributed in position over the telescope aperture, all with the same off-axis angles (polar and azimuthal) chosen by the user. For a point source at XRCF, rays originate at the source location and are uniformly distributed in direction over an annulus appropriate for the chosen mirror shell. For the FCM, the rays are uniformly distributed in position and direction. The effects of FCM non-uniformity are taken into account in post-processing where individual rays are appropriately weighted according to the FCM uniformity maps (§1.2). In position, the rays originate from within a circle whose radius, chosen by the user, may be larger than the FCM source radius. By noting the recorded initial ray position, the post-processing code can then handle multiple FCC locations using rays from the same run. In direction the rays are limited to a maximum off-axis polar angle chosen by the user. This angle must be large enough to encompass all rays that could reach the region of interest at the detection surface.

A.2.3 Collimators and central aperture plate

Propagation through the thermal pre-collimator, central aperture plate, and thermal post-collimator is handled by straightforward tracing of a straight line along the ray path. Any intersections with plates or struts terminate the ray.

A.2.4 Paraboloid and hyperboloid

Propagation through the paraboloid and hyperboloid are handled by searching for an intersection of ray and mirror, calculating the surface normal and grazing angle at the intersection point, reflecting the ray off the mirror into the appropriate specular direction, and propagating the ray to the end of the mirror. Mirror tilt and despace are applied to the incoming ray before searching for an intersection point, and then removed from the outgoing ray after reaching the end of the mirror. Figure errors are included using a first order perturbation method. First the code finds the intersection with the ideal surface and then corrects to first order in the figure errors. Figure errors are also included in the calculation of the reflected ray direction. Rays that miss either mirror are terminated. The code counts the number of such ghost rays, but does not record them for further analysis. Rays that strike the baffle in the paraboloid of shell 6 are of course also terminated.

A.2.5 Record ray at nominal focus

Doubly reflected rays that pass through the all collimators are propagated to the nominal focus ($X = 0$). Their position, direction, and both grazing angles are then written to a file. In the case of the FCM sources, the initial ray position on the FCC is also written to the file. Upon completion of the run, a summary of the run is recorded.

A.3 Scattering

Scattering from the mirror surfaces in non-specular directions is energy dependent. In order to run large numbers of rays in as short a time as possible, the Project Science ray trace code is designed to carry out energy dependent calculations during post-processing. In principle this procedure should be very accurate for predicting total effective areas and the core of the point-spread-function (PSF), but is less than ideal for scattering which is probably best accounted for during the ray trace run. However, this requires including energy dependences on reflectivity and on scattering through extensive scattering tables, and can be very costly in computer time. Non-specular scattering is important only for the wings of the PSF and for many purposes can be included in post-processing through convolution techniques. For example, it is possible to predict the structure of the PSF wings from knowledge of the high-frequency surface roughness of the mirrors and of the scattering from dust particles without a ray trace [10]. Convolution of the predicted wing and core PSFs then produces a combined predicted PSF.

A.4 Post-processing

A.4.1 FORTRAN

Using the results of the geomtric ray trace to calculate effective areas (without scattering effects) or FCM images (and compare them to FCM data) are post-processing tasks involving extensive numerical calculations of energy dependent reflectivity at two grazing angles for each ray reaching the focal plane. Project Science therefore uses FORTRAN code running on the SGI ORIGIN computer at MSFC to complete these tasks. Reflectivity calculations use an exact recursive algorithm [11], suitable for multilayer coatings, to model the AXAF coatings consisting of ~325 $\AA$ of ~95% bulk density iridium on ~100 $\AA$ of chromium on zerodur. Above 2 keV, the code uses optical constants for iridium supplied by MST and derived from synchrotron reflectance measurements [12] for iridium coated AXAF witness flats (we especially thank Dale Graessle and his team). All other optical constants come from Henke *et al* [13]. Using the effective area code, it is possible to:

1. Calculate effective areas integrated over the focal plane at large numbers of closely spaced energies.
2. Add a layer of some molecular contaminant (usually a hydrocarbon) on top of the AXAF coatings to study its effects on effective area.
3. Study the effects on effective area of density gradients, in the direction normal to the surface, in the coatings.

Using the FCM code with results from geometric ray traces for each FCM source and each shell, it is possible to:

1. Calculate the expected HRMA/ACIS image of the FCM system as a function of energy and, by noting the initial position of rays, of FCC position.
2. Correlate the predicted images as a function of FCC position with measured images.
3. Study the effects of FCM position tolerances and uniformity map misalignment on the FCC registration results.

A.4.2 *Mathematica*™

The symbolic mathematics package *Mathematica*™has proven very useful for a number of tasks, especially:

1. Development of algorithms.
2. Graphical display of results.

For the FCM registration analysis, a *Mathematica*™notebook is used to refine the correlation results produced by the FORTRAN code by interpolation between grid points, to determine errors, and to display results.

B Fitted FCM line rates at 2.984, 3.198, 5.895, and 6.490 keV

Table 9: Fitted rates for Ag Lα at E = 2.982 keV.

segment	0	1	2	3	segment	0	1	2	3
amplifier	CCD I0				amplifier	CCD I1			
0	0.0139	0.0266	0.0404	0.0611	0	0.136	0.141	0.131	0.127
1	0.0199	0.0314	0.0432	0.0671	1	0.137	0.138	0.129	0.109
2	0.0218	0.0369	0.0583	0.0832	2	0.137	0.133	0.128	0.105
3	0.0320	0.0449	0.0649	0.0933	3	0.136	0.130	0.117	0.0919
	CCD I2					CCD I3			
0	0.0468	0.0583	0.0765	0.106	0	0.162	0.171	0.174	0.177
1	0.0604	0.0790	0.0992	0.125	1	0.141	0.155	0.162	0.162
2	0.0841	0.102	0.126	0.147	2	0.139	0.152	0.145	0.143
3	0.116	0.131	0.159	0.176	3	0.138	0.137	0.142	0.132
	CCD S2					CCD S3			
0	0.152	0.158	0.153	0.156	0	0.271	0.280	0.274	0.245
1	0.183	0.187	0.187	0.173	1	0.269	0.270	0.278	0.264
2	0.218	0.233	0.216	0.198	2	0.268	0.272	0.277	0.266
3	0.236	0.236	0.241	0.234	3	0.245	0.256	0.252	0.242

Table 10: Fitted rates for Ag Lβ series at E = 3.198 keV.

segment	0	1	2	3	segment	0	1	2	3
amplifier	CCD I0				amplifier	CCD I1			
0	0.0146	0.0267	0.0415	0.0694	0	0.136	0.151	0.142	0.128
1	0.0203	0.0295	0.0512	0.0723	1	0.135	0.147	0.140	0.112
2	0.0260	0.0376	0.0567	0.0803	2	0.137	0.145	0.135	0.107
3	0.0328	0.0455	0.0728	0.0997	3	0.140	0.141	0.126	0.0924
	CCD I2					CCD I3			
0	0.0440	0.0643	0.0879	0.109	0	0.163	0.178	0.179	0.180
1	0.0666	0.0810	0.105	0.131	1	0.149	0.153	0.163	0.166
2	0.0922	0.111	0.133	0.154	2	0.148	0.150	0.150	0.152
3	0.117	0.141	0.163	0.174	3	0.138	0.144	0.150	0.134
	CCD S2					CCD S3			
0	0.154	0.166	0.159	0.152	0	0.286	0.275	0.255	0.231
1	0.197	0.190	0.192	0.181	1	0.282	0.283	0.257	0.232
2	0.232	0.231	0.217	0.211	2	0.279	0.276	0.264	0.228
3	0.249	0.244	0.249	0.244	3	0.265	0.259	0.242	0.209

Table 11: Fitted rates for Mn Kα at E = 5.895 keV.

segment	0	1	2	3	segment	0	1	2	3
amplifier	CCD I0				amplifier	CCD I1			
0	0.0221	0.0450	0.0904	0.177	0	0.553	0.586	0.557	0.455
1	0.0245	0.0507	0.107	0.205	1	0.567	0.591	0.550	0.413
2	0.0320	0.0657	0.130	0.240	2	0.575	0.588	0.506	0.373
3	0.0439	0.0788	0.154	0.290	3	0.592	0.567	0.464	0.328
	CCD I2					CCD I3			
0	0.0720	0.111	0.203	0.346	0	0.558	0.652	0.684	0.694
1	0.117	0.170	0.265	0.420	1	0.540	0.608	0.617	0.600
2	0.219	0.276	0.376	0.500	2	0.529	0.576	0.586	0.558
3	0.352	0.431	0.531	0.627	3	0.538	0.592	0.573	0.499
	CCD S2					CCD S3			
0	0.563	0.622	0.631	0.592	0	0.941	0.947	0.890	0.754
1	0.729	0.765	0.729	0.694	1	0.935	0.942	0.900	0.790
2	0.910	0.956	0.892	0.829	2	0.910	0.937	0.887	0.758
3	1.03	1.05	1.04	0.982	3	0.807	0.823	0.793	0.648

Table 12: Fitted rates for Mn Kβ1 at E = 6.490 keV.

segment	0	1	2	3	segment	0	1	2	3
amplifier	CCD I0				amplifier	CCD I1			
0	0.00116	0.00185	0.00420	0.0137	0	0.0510	0.0545	0.0528	0.0372
1	0.00205	0.00419	0.00682	0.0161	1	0.0591	0.0553	0.0497	0.0327
2	0.00139	0.00420	0.00910	0.0160	2	0.0568	0.0581	0.0452	0.0277
3	0.00340	0.00551	0.0123	0.0206	3	0.0575	0.0566	0.0393	0.0222
	CCD I2					CCD I3			
0	0.00533	0.00676	0.0134	0.0276	0	0.0495	0.0588	0.0604	0.0621
1	0.00638	0.0107	0.0187	0.0343	1	0.0498	0.0580	0.0579	0.0527
2	0.0163	0.0197	0.0277	0.0406	2	0.0477	0.0629	0.0553	0.0500
3	0.0275	0.0299	0.0402	0.0532	3	0.0513	0.0550	0.0548	0.0410
	CCD S2					CCD S3			
0	0.0431	0.0548	0.0632	0.0575	0	0.0993	0.0847	0.0718	0.0554
1	0.0559	0.0663	0.0791	0.0605	1	0.101	0.0922	0.0780	0.0554
2	0.0828	0.0847	0.0788	0.0738	2	0.0983	0.0890	0.0709	0.0552
3	0.0918	0.0932	0.0964	0.0912	3	0.0848	0.0717	0.0609	0.0488

References

[1] S. L. O'Dell and M. C. Weisskopf, "Advanced X-ray Astrophysics Facility (AXAF): Calibration overview," in *X-Ray Optics, Instruments, and Missions*, R. B. Hoover and A. B. Walker, eds., *Proc. SPIE* **3444**, pp. 2–18, 1998.

[2] P. Zhao, R. A. Austin, R. J. Edgar, R. F. Elsner, T. J. Gaetz, D. Jerius, J. J. Kolodziejczak, W. C. McDermott, S. L. O'Dell, M. E. Sulkanen, D. A. Schwartz, D. A. Swartz, A. F. Tennant, L. P. Van Speybroeck, B. J. Wargelin, M. C. Weisskopf, and G. Zirnstein, "AXAF mirror effective-area calibration using the C-continuum source and solid-state detectors," in *X-Ray Optics, Instruments, and Missions*, R. B. Hoover and A. B. Walker, eds., *Proc. SPIE* **3444**, pp. 234–257, 1998.

[3] R. F. Elsner, M. K. Joy, S. L. O'Dell, B. D. Ramsey, and M. C. Weisskopf, "Ground-to-orbit transfer of the AXAF-I flux scale: In-situ contamination monitoring of x-ray telescopes," in *Multilayer and grazing incidence X-ray/EUV optics for astronomy and projection lithography*, R. B. Hoover and A. B. Walker, eds., *Proc. SPIE* **2279**, pp. 332–342, 1994.

[4] E. Browne and R. B. Firestone, *Table of Radioactive Isotopes*, John Wiley and Sons, New York, 1986.

[5] J. A. Bearden, "X-ray wavelengths," *Rev. Mod. Phys.* **39**, pp. 78–124, 1967.

[6] F. Schwab, "Radiation Source Position." Eastman-Kodak Tech Note No. AXAF-96-0251-SCHWAB, November 8 1997.

[7] R. J. Edgar, L. P. David, T. J. Gaetz, D. Jerius, D. A. Schwartz, J. Everett, P. Zhao, L. M. Cohen, and W. A. Podgorski, "XRCF Phase 1 Testing: Preliminary Results." SAO-AXAF-DR-97-282, May 28 1997.

[8] W. H. Press, S. A. Teukolsky, W. T. Vetterling, and B. P. Flannery, *Numercial Recipes in FORTRAN, 2nd edition*, Cambridge University Press, Cambridge, 1992.

[9] D. Jerius, "Comparison of Project Science and MST Effective Area Simulations." SAO/MST memorandum, March 13 1997.

[10] S. L. O'Dell, R. F. Elsner, J. J. Kolodziejczak, M. C. Weisskopf, J. P. Hughes, and L. P. Van Speybroeck, "X-ray evidence for particulate contamination on the AXAF VETA-1 mirrors," in *Multilayer and grazing incidence X-ray/EUV optics for astronomy and projection lithography*, R. B. Hoover and A. B. Walker, eds., *Proc. SPIE* **1742**, pp. 171–182, 1993.

[11] R. F. Elsner, S. L. O'Dell, and M. C. Weisskopf, "Effective area of the axaf x-ray telescope: Dependence upon dielectric constants of coating materials," *J. X-ray Sci. and Tech.* **3**, pp. 35–44, 1991.

[12] D. E. Graessle, A. J. Burek, J. J. Fitch, B. Harris, D. A. Schwartz, and R. L. Blake, "Optical constants from synchrotron reflectance measurements of AXAF witness mirrors 2–12 keV," in *Grazing Incidence and Multilayer X-Ray Optical Systems*, R. B. Hoover and A. B. Walker, eds., *Proc. SPIE* **3113**, pp. 52–64, 1997.

[13] B. L. Henke, E. M. Gullikson, and J. C. Davis, "X-ray interactions: Photoabsorption, scattering, transmission, and reflection at E = 50–30000 eV, Z = 1–92," *Atomic Data & Nuclear Data Tables* **54**, pp. 181–342, 1993.